nature chemistry

SUPPLEMENTARY INFORMATION

https://doi.org/10.1038/s41557-018-0004-0

In the format provided by the authors and unedited.

Observation of correlated excitations in bimolecular collisions

Zhi Gao[1,2], Tijs Karman[1,2], Sjoerd N. Vogels[1], Matthieu Besemer[1], Ad van der Avoird[1], Gerrit C. Groenenboom[1*] and Sebastiaan Y. T. van de Meerakker[1*]

[1]Institute for Molecules and Materials, Radboud University, Nijmegen, The Netherlands. [2]These authors contributed equally: Zhi Gao and Tijs Karman.
*e-mail: gerritg@theochem.ru.nl; basvdm@science.ru.nl

Observation of correlated excitations in bimolecular collisions

Zhi Gao, Tijs Karman, Sjoerd N. Vogels, Matthieu Besemer, Ad van der Avoird, Gerrit C. Groenenboom* and Sebastiaan Y.T. van de Meerakker*

Radboud University, Institute for Molecules and Materials
Heijendaalseweg 135, 6525 AJ Nijmegen, the Netherlands
E-mail: gerritg@theochem.ru.nl, basvdm@science.ru.nl

Contents

1 Experimental methods

The experiments were performed using a crossed molecular beam apparatus which has been described previously [1, 2] and is shown schematically in Fig. 1. Here we only describe the essential part for this experiment. A mixture of 5% NO seeded in Kr at a typical pressure of 1 bar is expanded through a Nijmegen Pulsed Valve (NPV)[3] and subsequently enters a Stark decelerator. The NO($X\,^2\Pi_{1/2}, j_{\mathrm{NO}} = 1/2, f$) [hereafter denoted NO($1/2f$)] package was selected by the Stark decelerator with a speed of 450 m/s. After exiting the decelerator and 69 mm free flight, the package of NO collides with another package of O_2 molecules at 45° angle of incidence.

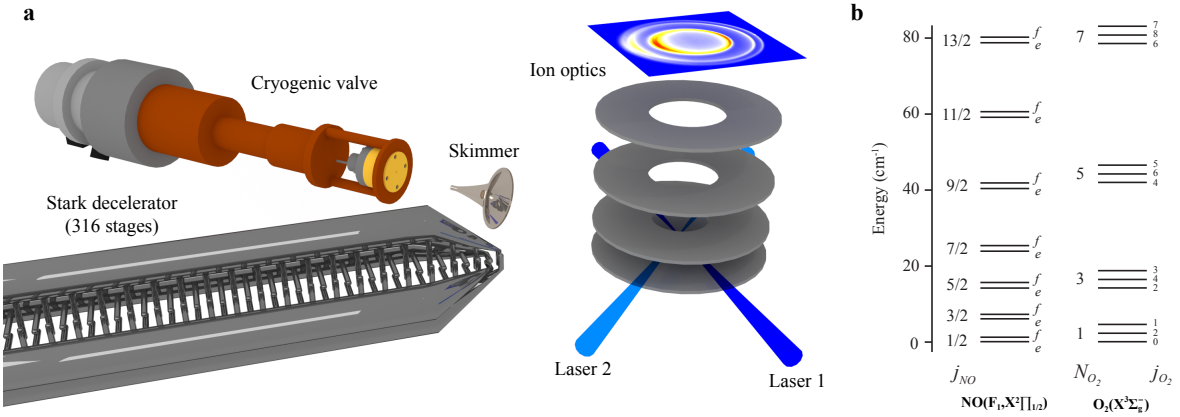

Figure 1: **Schematic representation of the experimental set-up. a:** The NO radical beam passes through a Stark decelerator and is scattered with a pulsed beam of O_2 at 45° angle of incidence. The inelastically scattered NO radicals are state-selectively ionized using two pulsed lasers, and detected using velocity map imaging. Only the last section of the Stark decelerator is shown. **b:** The rotational energy diagram of NO($X\,^2\Pi_{1/2}$) and O_2. The NO Λ-doublet splitting and O_2 fine-structure splittings are exaggerated for clarity.

A (1+1′) resonance enhanced multiphoton ionization (REMPI) scheme was used to state-selectively detect the reagent and scattered NO radicals using two pulsed dye laser systems. The Velocity Map Imaging (VMI) optics is used to collect the NO ions after the ionization. The ion optics used in the experiment consists of three extractor plates as used by Suits and coworkers [4], The grounded time of flight (TOF) tube has a length of 1100 mm, and the voltage applied on repeller and extractor plates are 3000V, 2755V, 2519V, 2160V respectively. The collision energy was calibrated using the method described in Refs. [2, 1, 5]. The pixel-to-m/s conversion factor of the VMI setup was calculated by using the extremely well calibrated velocities of NO radicals which emerge from the Stark decelerator. From the radii of the scattering images, we can determine the mean collision energy to be 160 cm^{-1}.

The O_2 beam was produced by expanding pure O_2 with a backing pressure of 5 bar into vacuum using a room temperature Even-Lavie valve [6]. In order to determine the initial rotational state distribution of the O_2 pulsed beam, a (2+1) REMPI spectrum of O_2 was measured. Figure 2 compares the (2+1) REMPI spectrum measured to calculations using PGOPHER [7] using a rotational temperature of 4K. The $O_2(X^3\Sigma_g^-)$ rotational energy levels are split by spin-spin and spin-rotation coupling [8]. This lifts the degeneracy of the fine-structure states labeled by the total angular momentum quantum number $j_{O_2} = N_{O_2} - 1$, N_{O_2}, and $N_{O_2} + 1$, which arises as the vector sum of rotational and electronic spin angular momenta, $\boldsymbol{j}_{O_2} = \boldsymbol{N}_{O_2} + \boldsymbol{S}_{O_2}$.

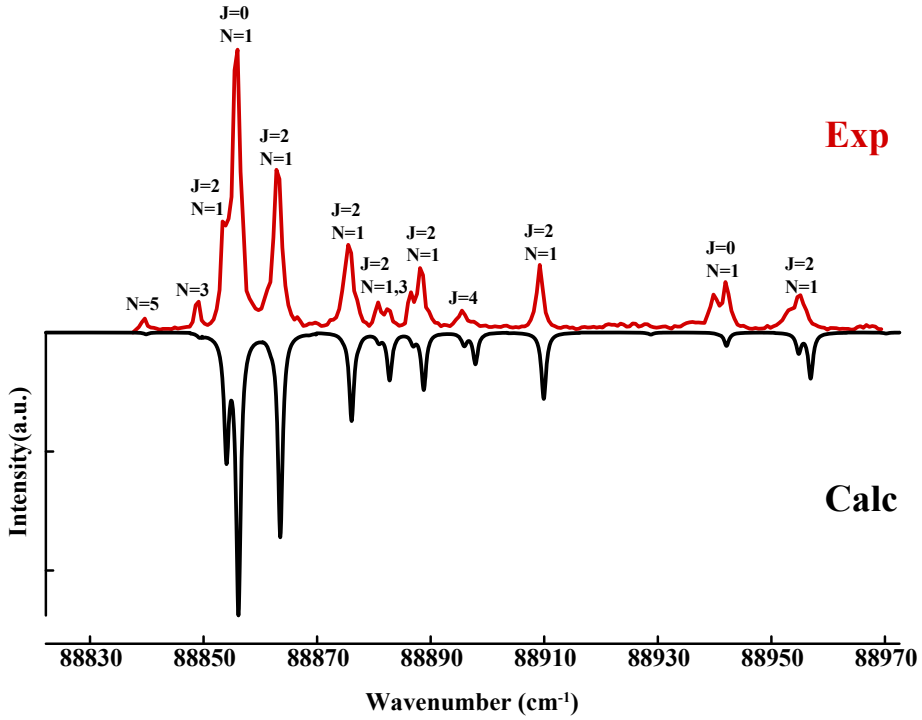

Figure 2: **(2+1) REMPI of** O_2. **Exp**: Experimental REMPI spectrum of O_2, **Calc**: PGOPHER-calculated REMPI spectrum of O_2. The assignment of the peaks is indicated by the values above the peaks. J is the total molecular angular momentum and N is nuclear rotational angular momentum.

From the comparison of the measured and calculated REMPI spectra, one can conclude that the O_2 molecules emerge from the Even-Lavie valve predominantly reside in the rotational state $N_{O_2} = 1$. The population of the fine-structure levels $j_{O_2} = 0$, 1, 2 follows a Boltzmann

distribution

$$P_j = (2j+1)\exp\left(-\frac{E_j}{kT}\right)/Q,$$
$$Q = \sum_j (2j+1)\exp\left(-\frac{E_j}{kT}\right) \quad (1)$$

where the temperature $T = 4$ K, k is the Boltzmann constant, and Q is the partition sum. In the above, P_j, E_j, and $2j+1$ are the population, energy, and degeneracy of the $j_{\mathrm{O}_2} = j$ level, respectively. The resulting populations of $j_{\mathrm{O}_2} = 0$, 1, 2 are 23%, 18%, and 59%, respectively.

2 Analysis and simulation

2.1 Assignment of the collision induced excitations in O_2

The images are analyzed as described below (see Figure 3 for an example). Multiple rings are observed in the scattering images. In order to assign the rotational state transitions of O_2, the radial scattering intensity distribution is analyzed for the angular range in between the two red dashed traces (from -20° to -10°) by a home-written MATLAB code.[9]. As a result of a variety of experimental and kinematic reasons, the highest scattering intensity in combination with optimal radial resolution is found in this region. We calculate the expected radii of the rings by energy and momentum conservation. As we cannot resolve excitation into individual j_{O_2} fine-structure states in O_2, we take for each N state of O_2 the average value for the NO($1/2f$) + $\mathrm{O}_2(N_{\mathrm{O}_2} = 1, j_{\mathrm{O}_2}) \rightarrow$ NO(j'_{NO}) + $\mathrm{O}_2(N'_{\mathrm{O}_2}, j'_{\mathrm{O}_2})$ excitation energies. It is seen that the highest intensities of the radial distributions shift 1 to 2 pixels inward with respect to the nearest dash line. These shifts stem from the projection of a three-dimensional Newton sphere onto a two-dimensional plane, and from the velocity spread of O_2 beam.

In the experimental images, it was observed that different rings in a single image have slightly different center points. A deviation of up to a few pixels is observed in the horizontal direction, but no deviations are observed in the vertical direction. The exact origin of this deviation is at present unknown, but is in part attributed to the imperfect mapping of velocities by our ion optics (in particular nonlinearity with respect to velocity). This hypothesis is supported by ion trajectory simulations of the detector geometry.

2.2 Simulation method

Images from full simulations of the experiment are obtained to compare with the experimental results. The detail of the simulations have been described elsewhere [5], here we only describe the essential part for this experiment. Since the majority of the O_2 molecules in the reagent beam populate the initial state $N_{\mathrm{O}_2} = 1$ state, only the $N_{\mathrm{O}_2} = 1$ initial states are considered in the simulation. We do, however, take the full $N_{\mathrm{O}_2}, j_{\mathrm{O}_2}$-resolved cross section into account

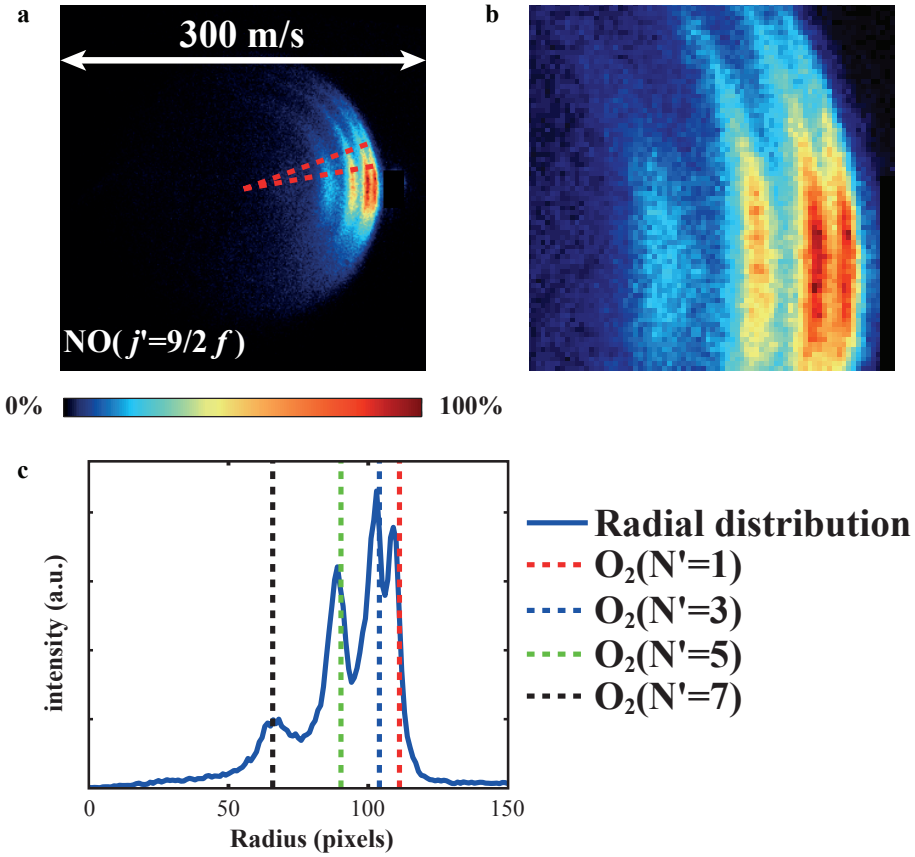

Figure 3: The radial distribution of scattering channel of $\mathrm{NO}(1/2\,f)\rightarrow\mathrm{NO}(9/2\,f)$. **a:** The raw scattering image with forward direction on the right side of the image. Small segments of the image around forward direction are masked because of imperfect state selection of NO package. The dash traces represent angular range of radial distribution. **b:** Zoom-in of the forward part in **a**. **c:** Radial distribution in **a**, the dash traces are used to compare radial distribution with energetically calculated radius for different final states of O_2.

as predicted by theory. For each of the three initial j_{O_2} states belonging to $N_{\mathrm{O}_2} = 1$, and for a given final state N'_{O_2}, we simulated the scattering image for the three possible $N_{\mathrm{O}_2} = 1, j_{\mathrm{O}_2} \rightarrow N'_{\mathrm{O}_2}, j'_{\mathrm{O}_2}$ transitions, and added them according to the initial j_{O_2} population. A single simulated scattering image containing 4 $(j'_{\mathrm{NO}}, N'_{\mathrm{O}_2})$ product-pair rings was therefore constructed from a total of 36 $j_{\mathrm{O}_2} \rightarrow j'_{\mathrm{O}_2}$-resolved simulated scattering images.

2.3 Analysis of angular distribution

The angular distribution of each of the rings in the scattering images directly reflect the differential cross sections (DCSs) of the scattering process [2]. By integrating the scattering intensity in

a narrow annulus close to the rim of the image, the angular distribution of the scattering images were determined. For all scattering images, an annulus with the same width was used.

Figure 4 shows the comparison of the angular scattering distributions extracted from the experimental images (**Exp**) and the simulated images (**Sim**). It is seen that excellent agreement between experiment and theory is obtained. For a given final state of NO, progressively more sideward scattering is observed with increasing excitation in O_2. In the distributions pertaining to NO(7/2 f), O_2 (N=1,3,5), rainbow features can be seen in the angular scattering distributions.

3 NO-O_2 diabatic Potential Energy Surfaces

We have calculated potential energy surfaces (PESs) at two levels of theory: spin-unrestricted coupled-cluster with full inclusion of single and double excitations and perturbative triples [UCCSD(T)], as well as multi-reference configuration interaction (MRCI) including single and double excitations.

For both sets of potentials, we first optimized restricted active space (RAS) self-consistent field (RASSCF) wave functions, where we include configurations corresponding to $\pi^{*,3}$, as well as double and quadruple $\pi \rightarrow \pi^*$ excitations. Without including $\pi \rightarrow \pi^*$ excitations, we were unable to obtain smooth potentials. This is related to symmetry breaking associated with the strong correlation of π and π^* orbitals. Hence, the static correlation of $\pi \rightarrow \pi^*$ double excitations had to be included in the RASSCF wave function. These calculations were performed state-averaged over the two lowest states, which correlate asymptotically to the spatially degenerate components of the $X^2\Pi$ state of NO. The calculations were performed separately for the doublet and quartet spin states of the complex.

For the MRCI potentials, we subsequently perform configuration interaction calculations for the two lowest states of each spin-multiplicity, by allowing for single and double excitations from the RAS. Energies are computed including Davidson's size-consistency correction, and a remaining size-inconsistency is subtracted by computing interaction energies at 100 a_0. This yields MRCI "adiabatic" interaction energies, which were transformed to the diabatic representation – used in subsequent scattering calculations – using the multiple-property-based diabatization algorithm of Ref. [10]. As properties, we included the the orbital angular momentum and quadrupole moment, which were computed adiabatically using the MRCI wave functions.

Computing CCSD(T) potentials is less straightforward for this open-shell system, as the states of interest are not necessarily well-described by a single determinant, and the ground state is nearly degenerate such that a single-reference approach may fail. Nevertheless, the spin-stretched quartet state of the NO-O_2 system can be treated by coupled-cluster theory. To this end, we re-compute canonical orbitals for a two-configuration two-state calculation including only $\pi^{*,3}$ configurations, using the RASSCF orbitals. The two states differ only in occupation of the two NO π^* orbitals by a single electron, and hence can be brought in single-determinant form exactly using natural orbitals. Using canonical orbitals, the two states are

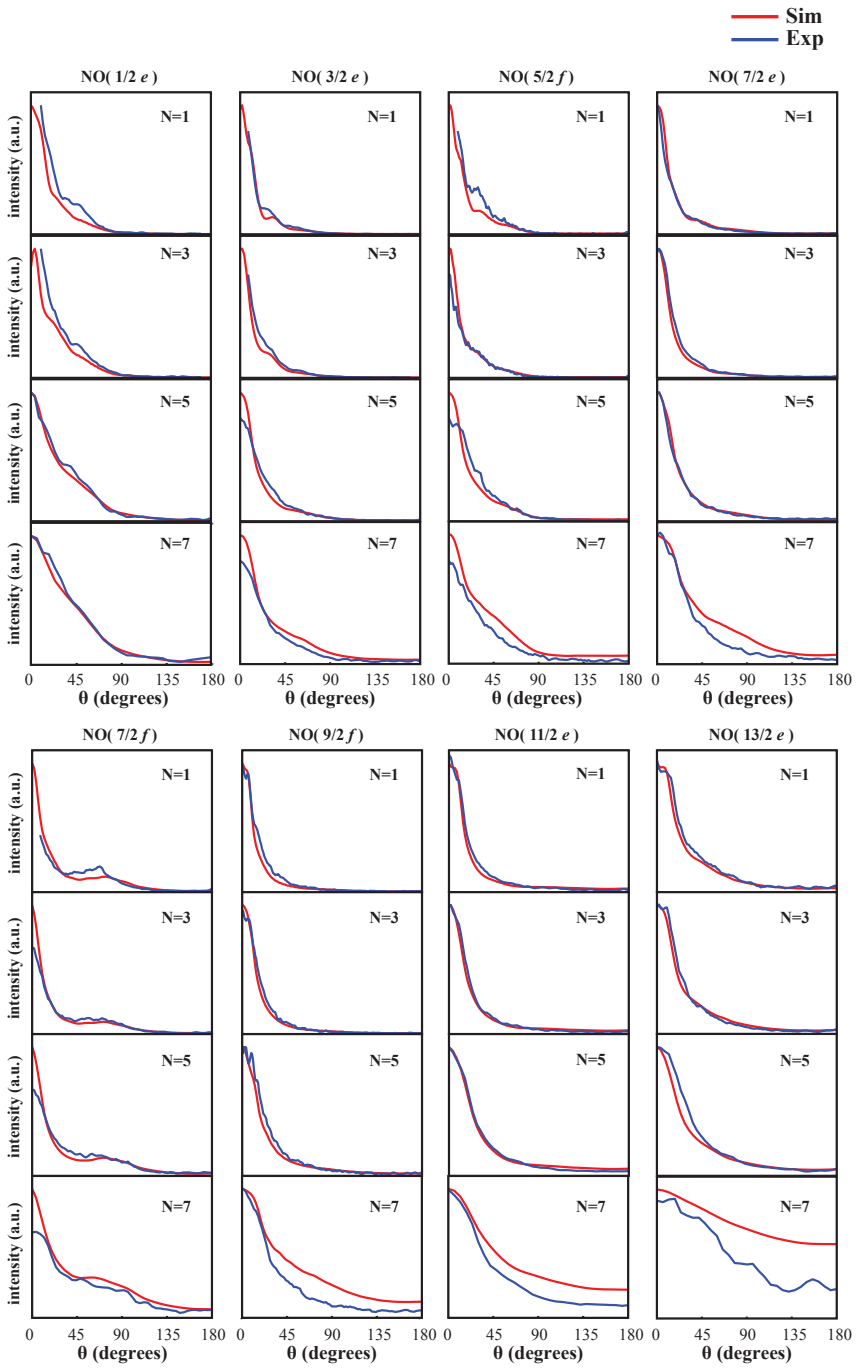

Figure 4: The comparison of angular scattering distribution derived from the experimental (**Exp**) and simulated (**Sim**) images.

generally close to single-determinant form. Subsequently, these single determinants can be used as reference wave functions in single-reference UCCSD(T) calculations. Mixing of the two nearly-degenerate states is included at the RASSCF level of theory, but higher-order mixing effects, at the correlated level, cannot be described by single-reference UCCSD(T). This approach is similar to what was used for the NO-H_2 potential of Ref. [11]. Properties in the adiabatic representation, used for diabatization, were computed using the single-determinant reference wave functions.

The calculated diabatic interaction energies were corrected for the basis-set superposition error (BSSE) as follows.[12] The interaction energies reported were computed by subtracting monomer energies, evaluated in the same one-electron basis set as used for the dimer calculations. Before applying the counterpoise correction, the adiabatic monomer states in the dimer basis set were transformed to the diabatic representation,[13, 11] using the same diabatization procedure.[10]

The Jacobi angles were sampled using 7 and 8 Gauss-Legendre quadrature points in $\theta_{\rm NO}$ and θ_{O_2}, The Jacobi coordinates are defined as in Fig. 1 of Ref. [14], where H_2 is to be replaced by O_2. respectively and 7 Gauss-Chebyshev quadrature points in ϕ. The radial grid consisted of points $R = 5, 5.5, 6, 6.5, 7, 7.5, 8, 8.5, 9, 9.5, 10, 11, 12, 13, 15, 20\ a_0$, and an additional point at $R = 100\ a_0$ which is used only to subtract the error in size-consistency. The vibrational coordinates are kept frozen at $r_{\rm NO} = 2.18\ a_0$ and $r_{\rm O_2} = 2.28\ a_0$. In total, this amounts to calculations for 3332 non-equivalent geometries. All calculations were performed using the MOLPRO 2012 suite of programs. The one-electron basis set consisted of aug-cc-pVTZ monomer-centered functions, supplemented by a set of mid-bond functions centered half-way the intermolecular axis. The mid-bond basis is an uncontracted Gaussian basis with exponents $sp(\alpha/3, \alpha, 3\alpha)$, $d(\alpha/\sqrt{3}, \alpha\sqrt{3})$, and $f(\alpha)$, where $\alpha = 20/R^2$.

The computational procedure outlined above yields two diabatic potentials, which are called diagonal and off-diagonal, respectively.[15] These have been expanded in angular functions, spherical harmonics and complex-conjugate Wigner D-matrix elements. The expansion coefficients were obtained using numerical integration over the Jacobi angles, using the Gauss-Legendre and Gauss-Chebyshev quadrature points.[15] The radial dependence of the resulting expansion coefficients was fit as follows. In the long-range, we explicitly fit terms with R^{-n} with $n \leq 6$ using a R^n-weighted linear least squares fit, using *ab initio* points with $R \geq 12$. We then obtain the short-range potential subtracting from the *ab initio* points the long-range potential as fit, and damped by multiplication with Tang-Toennies functions. These were fit using the reproducing kernel Hilbert space (RKHS) method, using smoothness parameter 2 and the asymptotic behavior set by the leading long-range term which was not fit explicitly. This process was performed separately for the UCCSD(T) potentials and MRCI potentials, and for both doublet and quartet spin-states. In the case of the UCCSD(T) potential, we used only the high-spin diagonal diabatic potentials.

Figure 5 shows the diabatic diagonal potentials calculated in this work, where the different panels correspond to different orientations of the two molecules. Although there are exceptions, the differences between the doublet and quartet potentials are relatively small for most orien-

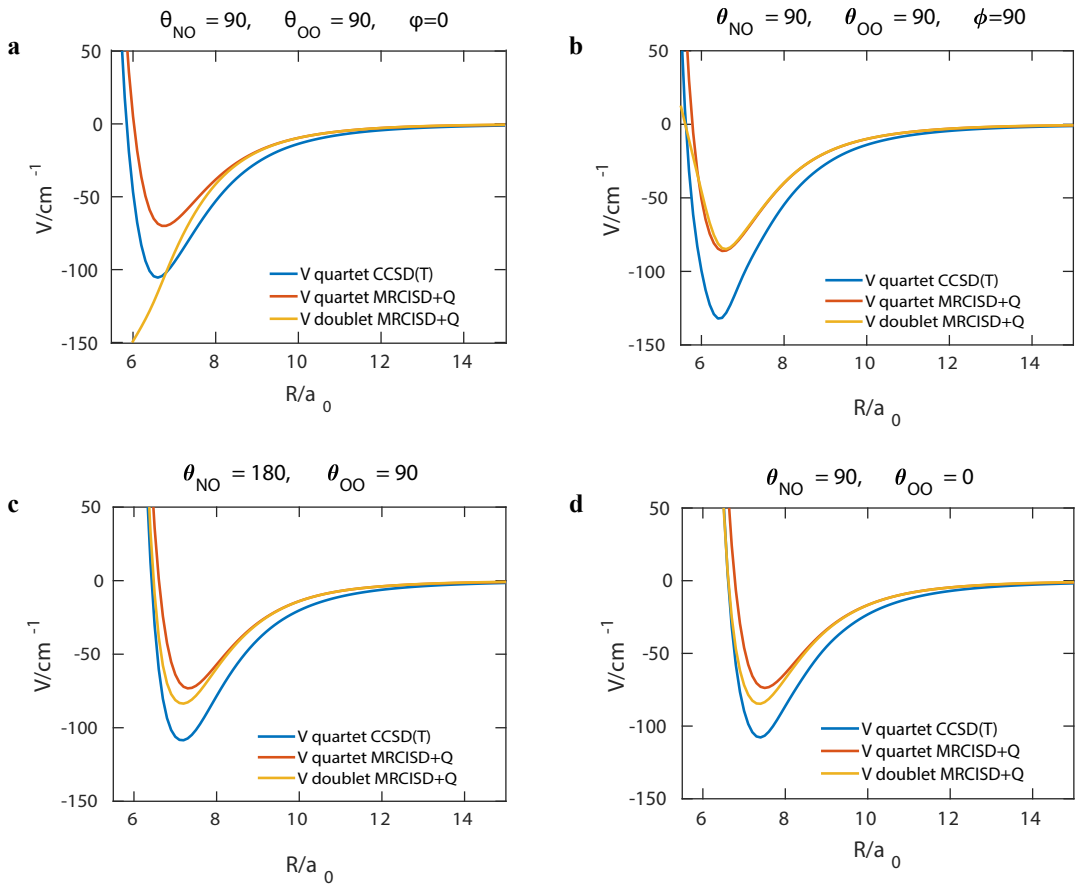

Figure 5: Diagonal diabatic potentials for different orientations, as indicated.

tations. The CCSD(T) potential is systematically deeper than the MRCI potential for the same quartet spin state, and this difference is typically larger than the splitting between the two spin states at the MRCI level. Because the CCSD(T) potential is assumed to be more accurate than the MRCI potential, and the CCSD(T) calculations can only be performed for the quartet spin state, this motivates to neglect the spin splittings and to use the CCSD(T) quartet potential as a spin-independent potential throughout. The approximation of a spin-independent potential also simplifies the subsequent scattering calculations.

Following the above motivation, we decide to use a set of coupled potential energy surfaces composed of the quartet diagonal potential computed at the UCCSD(T) level, and the quartet off-diagonal potential computed at the MRCI level of theory. Figure 6 shows the thus constructed *adiabatic* potentials for selected orientations of the molecules. These have been ob-

tained by evaluating the fit diabatic PESs, and subsequently diagonalizing the potential energy matrix.

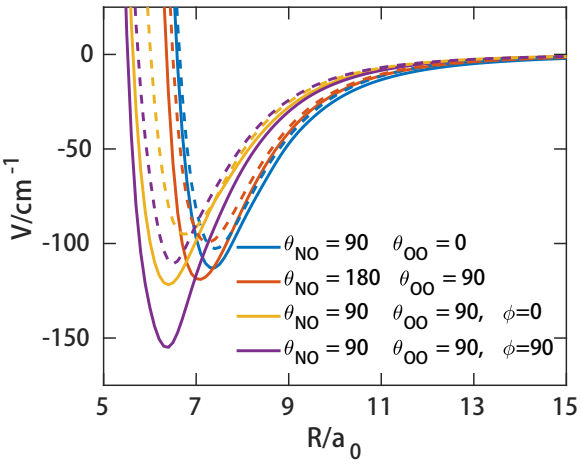

Figure 6: Radial dependence of the adiabatic potentials for selected orientations, as indicated by the color coding. The lower (upper) adiabatic state are shown as the solid (dashed) lines, throughout.

4 Scattering calculations

This section describes the details of the coupled-channels scattering calculations. In these calculations, we use the following Hamiltonian in atomic units

$$\hat{H} = -\frac{\hbar^2}{2\mu R}\frac{\partial^2}{\partial R^2}R + \frac{\hat{\ell}^2}{2\mu R^2} + \hat{H}_{\rm NO}(\boldsymbol{r}_{\rm NO}) + \hat{H}_{\rm O_2}(\boldsymbol{r}_{\rm O_2}) + \hat{V}(\boldsymbol{r}_{\rm NO}, \boldsymbol{r}_{\rm O_2}, \boldsymbol{R}), \tag{2}$$

where the vectors $\boldsymbol{r}_{\rm NO}$ and $\boldsymbol{r}_{\rm O_2}$ denote the orientations of the molecular axes of NO and O_2, respectively, the vector $\boldsymbol{R}$ connects the centers of mass of the molecules, R denotes the distance between the centers of mass, μ the reduced mass, $\hat{\boldsymbol{\ell}}$ the end-over-end angular momentum operator. The PES of the previous section is denoted $\hat{V}$. The monomer Hamiltonian of the NO molecule, $\hat{H}_{\rm NO}$, contains rotational kinetic energy, spin-orbit coupling, and Λ-doubling, as described elsewhere.[16] For the O_2 molecule, we include only rotational kinetic energy with rotational constant $B_{\rm O_2} = 1.438\ {\rm cm}^{-1}$, and neglect small spin-dependent couplings.

With the neglect of both the O_2 monomer spin-dependent couplings *and* the spin-dependence of the potential, the Hamiltonian of Eq. (2) is completely independent of the O_2 spin. Therefore, the dynamics is independent of the O_2 spin, and the O_2 monomer behaves effectively as a $^1\Sigma_g$ state molecule. The scattering wave function is then expanded in channel functions, which are

defined as follows

$$|([\epsilon_{\rm NO}\ \Omega_{\rm NO}\ j_{\rm NO}]N_{\rm O_2})j_{\rm AB}\ell;\mathcal{J}\mathcal{M}\rangle = \sum_{m_{\rm NO},M_{\rm O_2},m_{\rm AB},m_\ell} |\epsilon_{\rm NO}\ \Omega_{\rm NO}\ j_{\rm NO}\ m_{\rm NO}\rangle|N_{\rm O_2}M_{\rm O_2}\rangle|\ell m_\ell\rangle \times\langle j_{\rm NO}m_{\rm NO}N_{\rm O_2}M_{\rm O_2}|j_{\rm AB}m_{\rm AB}\rangle\langle j_{\rm AB}m_{\rm AB}\ell m_\ell|\mathcal{J}\mathcal{M}\rangle, \quad (3)$$

where $\langle j_1m_1j_2m_2|j_3m_3\rangle$ is a Clebsch-Gordan coefficient. Denoted by $|\epsilon_{\rm NO}\ \Omega_{\rm NO}\ j_{\rm NO}\ m_{\rm NO}\rangle$ is an NO eigenstate of $\hat{H}_{\rm NO}$, with parity $\epsilon_{\rm NO}$, total angular momentum $j_{\rm NO}$, space-fixed projection $m_{\rm NO}$, and approximate body-fixed projection $\Omega_{\rm NO} = +1/2, +3/2$. The state $|N_{\rm O_2}M_{\rm O_2}\rangle$ represents a rotational state of the "spin-less" $^1\Sigma_g$ $\rm O_2$ molecule. Due to permutation symmetry of indistinguishable Bosonic oxygen nuclei, only rotational states with odd $N_{\rm O_2}$ occur. Finally, the angular momentum ket $|\ell m_\ell\rangle$ describes the end-over-end rotation.

Inserting the coupled-channels expansion of the scattering wave function into the time-independent Schrödinger equation, and taking matrix elements in the channel basis defined above then yields the usual coupled-channels equations. The solution to the coupled-channels equations is propagated numerically using the renormalized Numerov method, from $R = 4.5$ in steps of 0.05 to 30 a_0. The channel basis was truncated by including only functions with $j_{\rm NO} \leq 17/2$ and $N_{\rm O_2} \leq 7$, and $\mathcal{J} \leq 201/2$. This amounts to channel bases of dimensions up to 6408. Without our approximations concerning the spin-dependence of the $\rm O_2$ monomer Hamiltonian and interaction potential, the dimension of the channel basis would have tripled, rendering the scattering calculations prohibitively computer intensive. Convergence was tested by comparing results of calculations with $\{j_{\rm NO}, N_{\rm O_2}\} \leq \{13/2, 7\}$ to those with $\{17/2, 9\}$ for only 20 values of $\mathcal{J}$, and both parities.

This yielded integral cross sections converged to about 20 % for most of the relevant channels, and typically much better for lower final states.

At $R = 30\ a_0$, where the intermolecular interaction vanishes, the asymptotic boundary conditions are imposed. This yields the S-matrices, from which differential scattering cross sections are obtained and compared to experimental results. The dynamics, and therefore the S-matrices, are independent of the $\rm O_2$ electron spin, but can still be used to compute $\rm O_2$ fine-structure resolved cross sections. Knowledge of the fine-structure resolved cross sections is useful for the simulations, described in Sec. 2.2, since the fine-structure splitting is in part responsible for blurring of the experimental images, and because the initial states are not statistically distributed over different fine structure levels.

To compute fine-structure-resolved cross sections, we first transform the S-matrix to an uncoupled representation, using Eq. (3). Next, we re-introduce the spectator spin degrees of freedom of the $\rm O_2$ molecule, and transform to the fine-structure basis using

$$|(N_{\rm O_2}S)j_{\rm O_2}m_{\rm O_2}\rangle = \sum_{M_{\rm O_2},M_S} |N_{\rm O_2}M_{\rm O_2}\rangle|SM_S\rangle\langle N_{\rm O_2}M_{\rm O_2}SM_S|j_{\rm O_2}m_{\rm O_2}\rangle. \quad (4)$$

This assumes that the $\rm O_2$ molecule is a pure Hund's case (b) molecule, consistent with the neglect of spin-dependent couplings in the monomer Hamiltonian, and neglects small mixing

of $N_{\mathrm{O}_2} = j_{\mathrm{O}_2} \pm 1$ for even j_{O_2}. We introduce the following composite quantum number $\boldsymbol{q} = \{\epsilon_{\mathrm{NO}}, \Omega_{\mathrm{NO}}, j_{\mathrm{NO}}, m_{\mathrm{NO}}, \ell, m_\ell\}$, describing all quantum numbers except for those pertaining to the O_2 molecule. Explicitly, one has for the fine-structure-resolved S-matrix elements

$$\begin{aligned}\tilde{S}_{(\boldsymbol{q}',[N',S,]j'_{\mathrm{O}_2},m'_{\mathrm{O}_2};\ \boldsymbol{q},[N,S,]j_{\mathrm{O}_2},m_{\mathrm{O}_2})} &= \sum_{M'_{\mathrm{O}_2},M'_S} \langle N'_{\mathrm{O}_2} M'_{\mathrm{O}_2} S M'_S | j'_{\mathrm{O}_2} m'_{\mathrm{O}_2}\rangle \\ &\sum_{M_{\mathrm{O}_2},M_S} S_{(\boldsymbol{q}',N',M'_{\mathrm{O}_2},S,M'_S;\ \boldsymbol{q},N,M_{\mathrm{O}_2},S,M_S)} \langle N_{\mathrm{O}_2} M_{\mathrm{O}_2} S M_S | j_{\mathrm{O}_2} m_{\mathrm{O}_2}\rangle \\ &= \sum_{M_S} S_{(\boldsymbol{q}',N',m'_{\mathrm{O}_2}-M_S,S,M_S;\ \boldsymbol{q},N,m_{\mathrm{O}_2}-M_S,S,M_S)} \\ &\times \langle N'_{\mathrm{O}_2}, m'_{\mathrm{O}_2} - M_S, S, M_S | j'_{\mathrm{O}_2} m'_{\mathrm{O}_2}\rangle \langle N_{\mathrm{O}_2}, m_{\mathrm{O}_2} - M_S, S, M_S | j_{\mathrm{O}_2} m_{\mathrm{O}_2}\rangle,\end{aligned} \tag{5}$$

where we have used that the S-matrix is O_2-spin independent, i.e., diagonal in M_S and independent of its value. Thus, we can thus drop the O_2-spin quantum numbers for compactness, $S_{(\boldsymbol{q}',N',M'_{\mathrm{O}_2},S,M_S;\ \boldsymbol{q},N,M_{\mathrm{O}_2},S,M_S)} \equiv S_{(\boldsymbol{q}',N',M'_{\mathrm{O}_2};\ \boldsymbol{q},N,M_{\mathrm{O}_2})}$, and identify these matrix elements with those obtained from the spin-independent calculations described above. This method can be called a "recoupling approach", and has previously been used to compute hyperfine-structure resolved cross sections, whilst treating the dynamics as independent of the nuclear spin degrees of freedom.[17]

5 Analysis

We recall that the integral cross section is given in terms of the T-matrix elements as

$$\begin{aligned}\sigma_{(\epsilon_{\mathrm{NO}},\Omega_{\mathrm{NO}},j_{\mathrm{NO}},N_{\mathrm{O}_2}\to\epsilon'_{\mathrm{NO}},\Omega'_{\mathrm{NO}},j'_{\mathrm{NO}},N'_{\mathrm{O}_2})} &= \frac{\pi}{(j_{\mathrm{NO}})(N_{\mathrm{O}_2})k^2} \\ &\sum_{j_{\mathrm{AB}},\ell,j'_{\mathrm{AB}},\ell',\mathcal{J}} (2\mathcal{J}+1) \left| T^{(\mathcal{J})}_{(\epsilon'_{\mathrm{NO}},\Omega'_{\mathrm{NO}},j'_{\mathrm{NO}},N'_{\mathrm{O}_2},j'_{\mathrm{AB}},\ell';\epsilon_{\mathrm{NO}},\Omega_{\mathrm{NO}},j_{\mathrm{NO}},N_{\mathrm{O}_2},j_{\mathrm{AB}},\ell)} \right|^2,\end{aligned} \tag{6}$$

where $(j) = 2j+1$ and $k = \sqrt{2\mu E}$ is the initial wave number. The idea is that one can identify the partial sum, restricted to a particular value of some of the quantum numbers ℓ, j_{AB}, and/or their primed counterparts, with the contribution of these quantum numbers to the total cross section. These partial cross sections are analyzed in this section, as they reveal valuable information about the underlying scattering dynamics.

We first turn our attention to the opacity functions, which are the contributions of specific initial relative angular momenta, ℓ. It is useful to identify ℓ with a classical impact parameter through $b = \ell/k$. We then define the opacity function as

$$P_{(\boldsymbol{i}\to\boldsymbol{f})}(b) = \frac{k}{2\pi b} \sigma^{(\ell)}_{(\boldsymbol{i}\to\boldsymbol{f})}(b), \tag{7}$$

where we introduce $\boldsymbol{i}$ and $\boldsymbol{f}$ as composite labels for the initial and final state quantum numbers, and the superscript on σ denotes the quantum numbers restricted in the partial cross section. The opacity function is a dimensionless quantity that is interpreted as the probability of excitation as a function of the impact parameter. With this definition, the cross section is given by

$$\sigma_{(\boldsymbol{i}\to\boldsymbol{f})} = \int_0^{2\pi} d\phi \int_0^{\infty} b\, db\, P_{(\boldsymbol{i}\to\boldsymbol{f})}(b), \tag{8}$$

in the classical limit of continuous b.

Opacity functions are shown in Fig. 7, where each panel corresponds to a specific final state of NO, and the four lines in each panel correspond to the four O_2 final states $N'_{O_2} = 1, 3, 5, 7$. A clear trend is observed, as with increasing inelasticity – higher-lying final states – the contributions to the cross sections become progressively more short ranged. This means that when one observes a single low-lying state of NO, channels with low N'_{O_2} have stronger long-range contributions than product pairs with high N'_{O_2} and hence dominate. If one observes a highly-excited NO state, the process is highly inelastic and short ranged irrespective of the O_2 final state, such that product pairs with high N'_{O_2} contribute significantly. The same trends are observed in Fig. 8, where each panel refers to a fixed O_2 final state, rather than a fixed NO final state.

Next we consider partial cross sections restricted to specific j_{AB} and j'_{AB}. We remind the reader that j_{AB} is introduced in the channel basis, Eq. (3), by coupling the fragment angular momenta, i.e., j_{AB} represents the magnitude of the vector sum $\boldsymbol{j}_{AB} = \boldsymbol{j}_{NO} + \boldsymbol{N}_{O_2}$. In the initial state, we have $j_{NO} = 1/2$ and $N_{O_2} = 1$, such that we have two possible values for $j_{AB} = 1/2$, and $3/2$. In Figs. 9 and 10, we show normalized partial cross sections restricted to $j_{AB} = 1/2$ and $j_{AB} = 3/2$, respectively, as a function of j'_{AB}, for various NO and O_2 final states. There is a clear propensity for j'_{AB} to assume the largest value permitted by the triangular inequalities, $j'_{AB} = j'_{NO} + N'_{O_2}$. This can be understood classically by considering for example a co-planar geometry as shown schematically in Fig. 11. If the nearest atoms of each molecule exert equal and opposite attractive (repulsive) forces on each other, both molecules will start to rotate in a clockwise (counter-clockwise) sense. The two molecules display the same sense of rotation, such that $\boldsymbol{j}_{NO}$ and $\boldsymbol{N}_{O_2}$ are parallel, and their vector sum, $\boldsymbol{j}_{AB}$, will assume the largest possible length.

Finally, we consider partial cross sections restricted to definite K'_{AB},the projection of j'_{AB} onto the intermolecular axis. To this end, we have transformed the space-fixed T-matrices to a body-fixed representation, and subsequently computed the partial cross section as a trace over all quantum numbers except for K'_{AB}. Resulting normalized partial cross sections are shown in Fig. 12. The cross sections clearly peak for low K'_{AB}. This can be understood as in the coupled-states approximation, which amounts to the neglect of Coriolis coupling, the quantum number K_{AB} is conserved, and the initial states have $K_{AB} = {}^1/_2$ or ${}^3/_2$. In the full coupled-channels calculation, K_{AB} is not conserved rigorously, but a propensity towards the coupled-states result $K'_{AB} = K_{AB}$ is clearly observed.

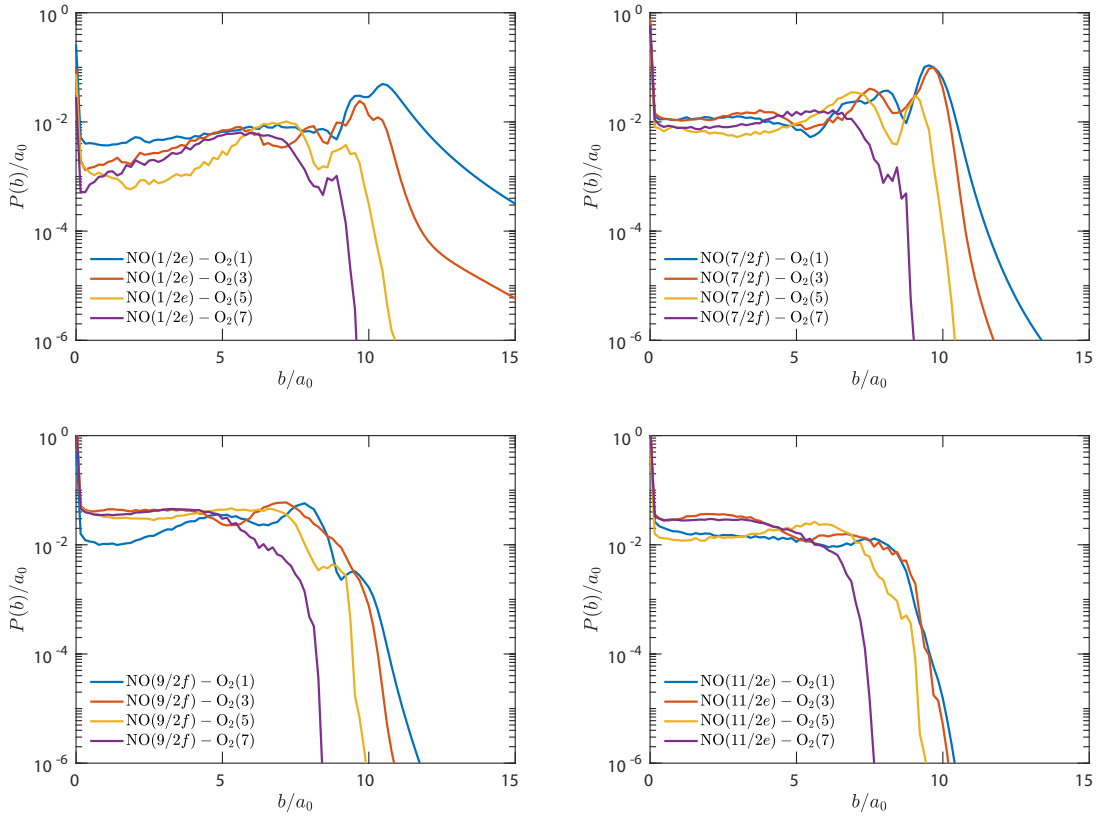

Figure 7: Opacity plots for $O_2(N'_{O_2} = 1, 3, 5, 7)$ and fixed NO final states, as indicated in the legend of each panel.

6 Entanglement

In this paper, we use classical correlations of two colliding molecules to determine the internal quantum state of the collision partner. One may wonder whether quantum correlations are also present. In particular, the non-zero angular momenta of two excited molecules may be entangled. Such entanglement is not measured experimentally, but we here investigate if such entanglement occurs for the calculated scattering wave functions.

To compute an entanglement measure from our scattering wave functions, we setup the asymptotic wave function in the basis of $(2j'_{NO} + 1)(2j'_{O_2} + 1)$ final states corresponding to a specific product pair, $NO(j'_{NO}) + O_2(N', j'_{O_2})$. From this, we set up the dimer and monomer

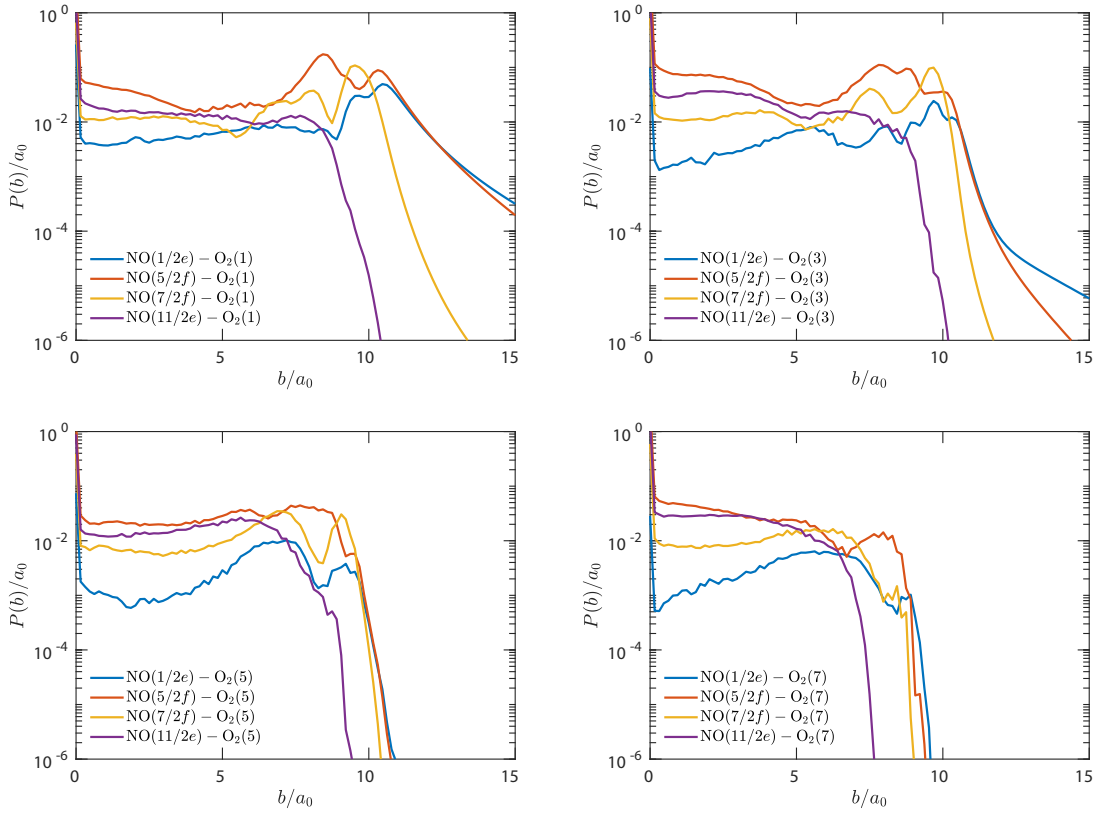

Figure 8: Opacity plots for NO $(j' = 1/2e)$ $(5/2f)$ $(7/2f)$ $(11/2e)$ and fixed O_2 final rotational levels, as indicated in the legend of each panel.

density matrices

$$\begin{aligned} \boldsymbol{\rho} &= |\Psi\rangle\langle\Psi|, \\ \boldsymbol{\rho}_A &= \mathrm{Tr}\,[\boldsymbol{\rho}]_B\,, \\ \boldsymbol{\rho}_B &= \mathrm{Tr}\,[\boldsymbol{\rho}]_A\,. \end{aligned} \tag{9}$$

In the above, Tr denotes the trace, and the subscript A or B denotes a restricted trace over the indicated monomer degrees of freedom only. We apply a scaling such that the full density matrix is normalized, $\mathrm{Tr}[\boldsymbol{\rho}] = 1$.

In the above, we have taken as the initial state $\mathrm{NO}(j_{\mathrm{NO}} = 1/2, m_{\mathrm{NO}} = +1/2)$ $\mathrm{O}_2(N = 1, j_{\mathrm{O}_2} = 0)$. In the experiment, the NO monomer is not polarized, such that $m_{\mathrm{NO}} = -1/2$ contributes equally, and $j_{\mathrm{O}_2} = 1, 2$ contribute as well. This simplification of using a pure initial state, however, allows us to simply consider the entanglement entropy as an entanglement

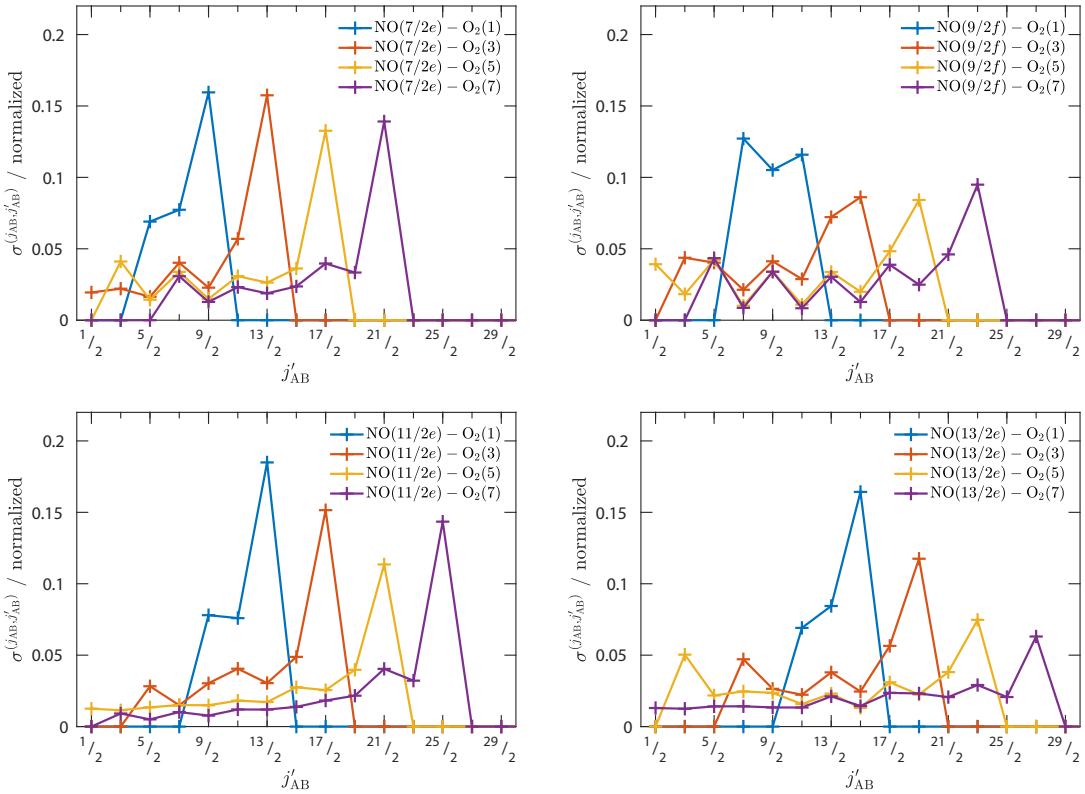

Figure 9: Normalized partial cross sections for $j_{\rm AB} = 1/2$ as a function of $j'_{\rm AB}$. The final states are indicated in the legends,where each panel correspond to a fixed NO state and shows data for the four O_2 final states $N'_{O_2} = 1, 3, 5, 7$.

measure

$$S(\boldsymbol{\rho}) = -\mathrm{Tr}\left[\boldsymbol{\rho} \ln\left(\boldsymbol{\rho}\right)\right], \\ E(\boldsymbol{\rho}) = S(\boldsymbol{\rho}) - S(\boldsymbol{\rho}_A) - S(\boldsymbol{\rho}_B). \tag{10}$$

This entropy vanishes if the two molecules are not entangled, i.e. are in a product state. The entropy equals $-2\ln(n)$, where $n = \min(2j'_{\rm NO}+1, 2j'_{O_2}+1)$, for a maximally entangled state.

Figure 13 shows an example of the entanglement entropy as a function of the scattering angle, normalized to the maximally-entangled value. The entanglement is generally non-zero and is a structured function of the scattering angle, except for $j'_{O_2} = 0$ final states which are necessarily un-entangled. The entanglement reaches about 80 % of the maximally entangled value.

To better understand the entanglement of the molecular angular momenta, we consider the following. In the previous section, we have shown that there is a propensity towards $j'_{\rm AB} = j'_A + j'_B$, and conservation of $K_{\rm AB}$, the body-fixed angular momentum. Given values of j'_A and

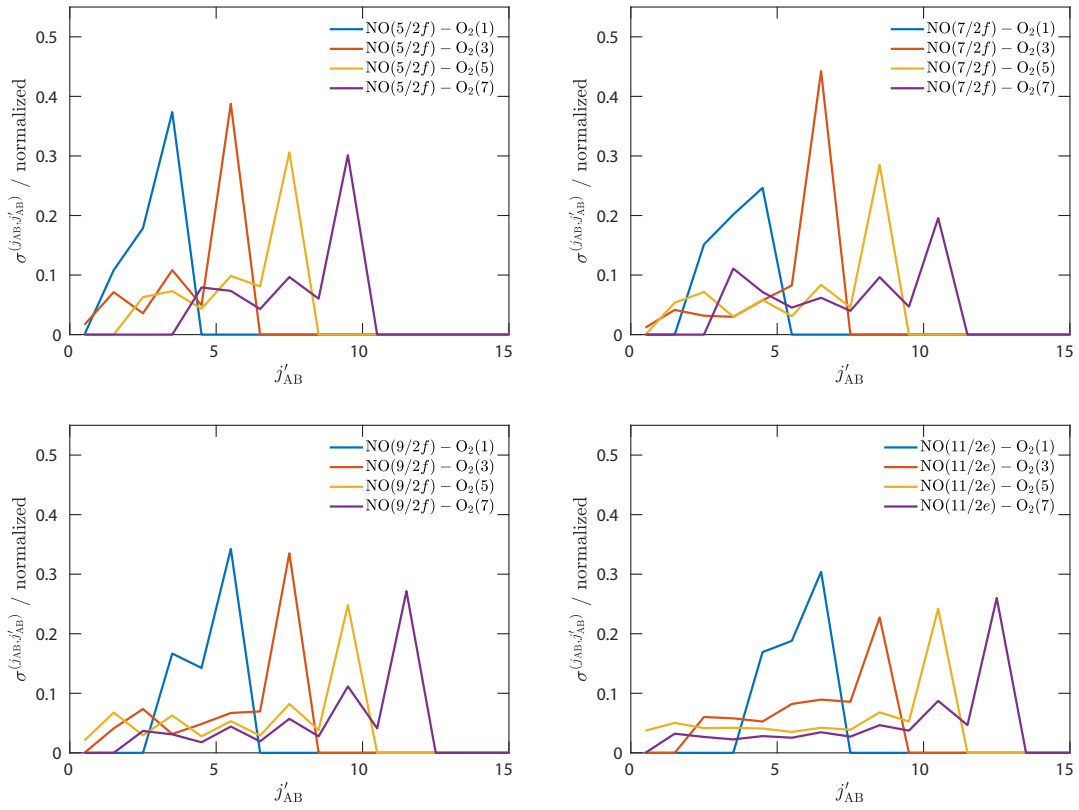

Figure 10: Normalized partial cross sections for $j_{\rm AB} = 3/2$ as a function of $j'_{\rm AB}$. The final states are indicated in the legends,where each panel correspond to a fixed NO state and shows data for the four O_2 final states $N'_{O_2} = 1, 3, 5, 7$.

j'_B, and a single initial value of $K_{\rm AB} = +1/2$, this completely determines the internal wave function of the complex,

$$|(j'_A j'_B) j'_{\rm AB} K'_{\rm AB}\rangle = \sum_{K'_A, K'_B} |j'_A K'_A\rangle |j'_B K'_B\rangle \langle j'_A K'_A j'_B K'_B | j'_{\rm AB} K'_{\rm AB}\rangle, \tag{11}$$

and we can compute the entanglement for this wave function from Eqs. (9) and (10). From this, we typically obtain entanglement entropies of around 60-80 % of the maximally entangled value, in agreement with the values obtained from the quantum scattering calculations. Now, there is only a propensity towards $j'_{\rm AB} = j'_A + j'_B$ and $\Delta K = 0$, such that the full wave function is not necessarily dominated by this component. Nevertheless, these simplified considerations give some insight into the mechanisms that generate entanglement in molecular collisions.

Next, we examine the possibility of finding violations of Bell inequalities. In the literature, Bell's original inequality,[18] formulated for two two-outcome measurements on two entangled particles, has been generalized further and improved upon many times. In particular, Collins

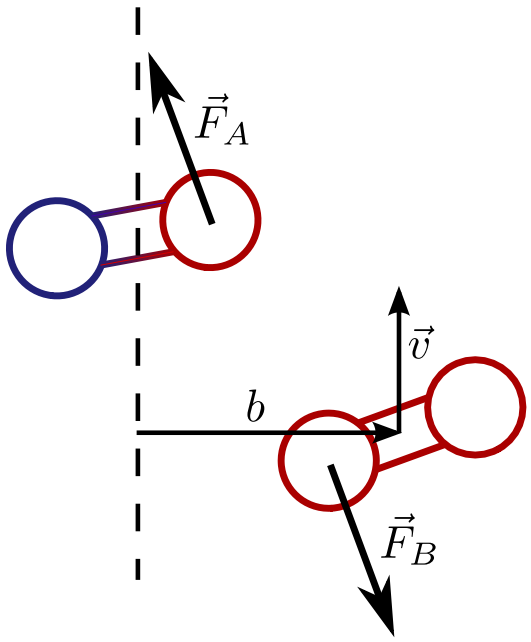

Figure 11: Schematic of a co-planar collision with repulsive interactions. The top-left molecule is drawn fixed, whilst the bottom-right molecule is drawn incident with velocity $\vec{v}$ at impact parameter b. Equal and opposite forces are exerted on the nearest atoms of each molecule,such that both molecules are excited rotationally with the same counter-clockwise sense of rotation.

et al.[19] have presented inequalities for two d-outcome measurements on two entangled particles that appear to be optimal for two photons that are maximally-entangled in d modes. Here, we use a simple CHSH inequality, described below, where the measured property is somewhat optimized for a given wave function. The reason for not using literature results for the Bell inequality is that NO has half-integer angular momentum, whereas O_2 has integer angular momentum, such that the dimension of the monomer Hilbert spaces, $2j + 1$, are necessarily unequal. To the best of our knowledge, Bell inequalities where $d_A \neq d_B$ are unavailable in the literature, except for special cases where d_A or $d_B = 2$.[20] A reason could be that the degree of entanglement always remains limited by the lowest of the two dimensions, such that it does not seem relevant to study the case $d_A \neq d_B$, except for in the present context of bimolecular scattering. Furthermore, the Bell inequalities in the literature are often violated for maximally-entangled photons, but it is not clear that they would also be close to optimal for molecular scattering.

An entangled quantum state, where subsystem A is described by the d_A quantum states

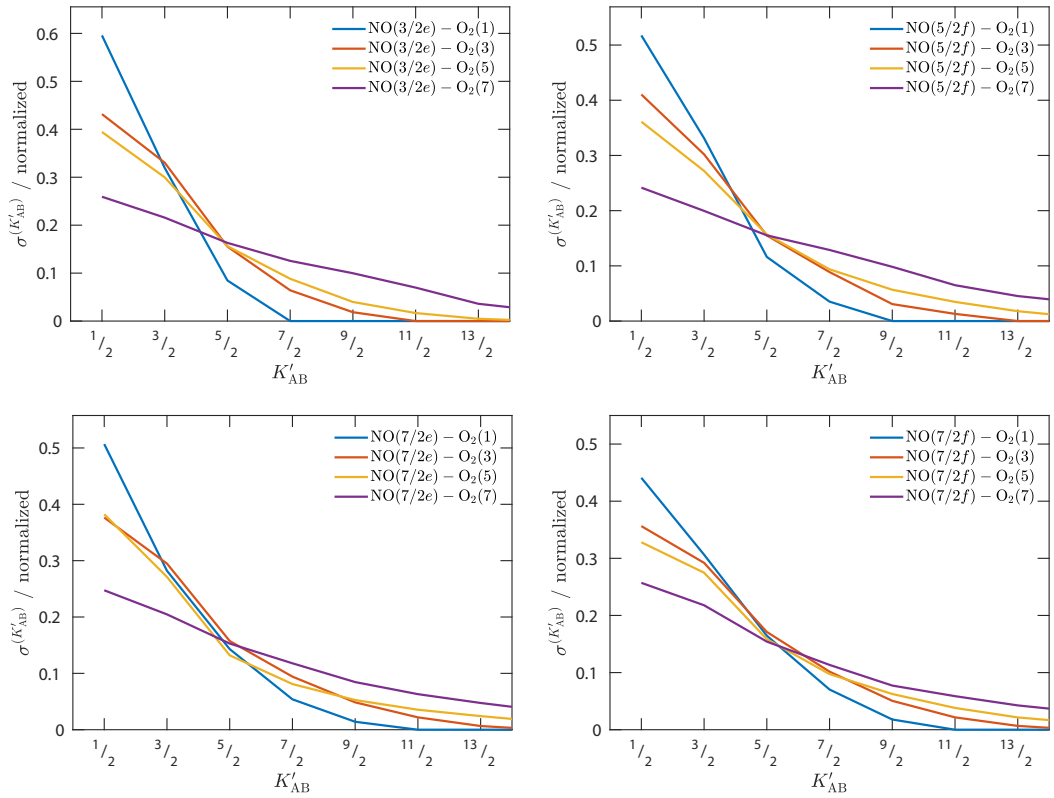

Figure 12: Normalized partial cross sections as a function of K'_{AB}, the body-fixed projection of angular momentum.The final states are indicated in the legends, where each panel correspond to a fixed NO state and shows data for the four O_2 final states $N'_{O_2} = 1, 3, 5, 7$.

$|i_A\rangle^{(A)}$ and subsystem B is described by the d_B quantum states $|i_B\rangle^{(B)}$, can be written as

$$|\Psi\rangle = \sum_{i_A=1}^{d_A} \sum_{i_B=1}^{d_B} c_{i_A,i_B} |i_A\rangle^{(A)} \otimes |i_B\rangle^{(B)}. \tag{12}$$

We use the singular value decomposition of the $d_A \times d_B$ matrix of expansion coefficients $\boldsymbol{c}$,

$$\boldsymbol{c} = \boldsymbol{L}\boldsymbol{\sigma}\boldsymbol{R}^{\dagger}, \tag{13}$$

where $\boldsymbol{\sigma}$ is a diagonal $d_A \times d_B$ matrix with the singular values σ_i, in decreasing order, on the diagonal, $\boldsymbol{L}$ is a $d_A \times d_A$ unitary matrix with left-singular vectors as columns, and $\boldsymbol{R}$ is a $d_B \times d_B$ unitary matrix of right-singular vectors. There are at most $d_< = \min(d_A, d_B)$ non-zero singular values. Non-entangled states, product states, have only one non-zero singular value, which is

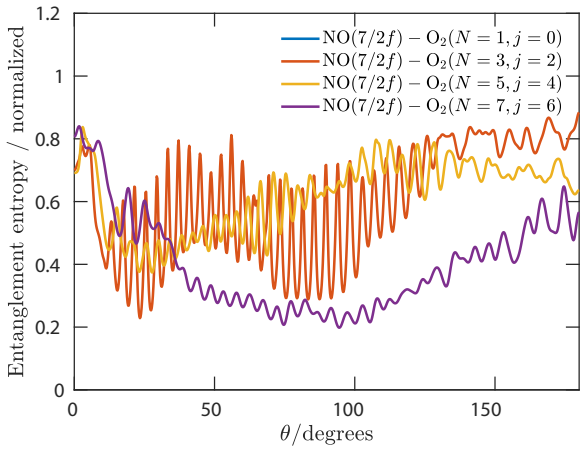

Figure 13: Entanglement entropy of Eq. (10) for scattering from a pure $\mathrm{NO}(j = 1/2, m = +1/2)$ $\mathrm{O}_2(N = 1, j = 0)$ state to the indicated final states. The entropy is normalized to the entropy of a maximally entangled state, $-2\ln(n)$, where $n = \min(2j'_{\mathrm{NO}} + 1, 2j'_{\mathrm{O}_2} + 1)$ is the smallest dimension of the monomer Hilbert spaces.

equal to unity. Now we can write the quantum state as

$$|\Psi\rangle = \sum_{i_\sigma=1}^{d_<} \sigma_{i_\sigma} |i_\sigma\rangle^{(A,\sigma)} \otimes |i_\sigma\rangle^{(B,\sigma)}, \tag{14}$$

with the A and B "singular states"

$$\begin{aligned} |i_\sigma\rangle^{(A,\sigma)} &= \sum_{i_A=1}^{d_A} L_{i_A,i_\sigma} |i_A\rangle^{(A)}, \\ |i_\sigma\rangle^{(B,\sigma)} &= \sum_{i_B=1}^{d_B} R^*_{i_B,i_\sigma} |i_B\rangle^{(B)}. \end{aligned} \tag{15}$$

If all singular values are equal, $\sigma_i = 1/\sqrt{d_<}$, this takes exactly the form of the maximally entangled state in $d_<$ modes.

We introduce the "spin" operators for molecules A and B, in terms of the singular states, as

$$\begin{aligned} \hat{S}_u^{(A)} &= \left[|1\rangle^{(A,\sigma)}, |2\rangle^{(A,\sigma)}\right] \boldsymbol{\sigma}_u \left[\langle 1|^{(A,\sigma)}, \langle 2|^{(A,\sigma)}\right]^T, \\ \hat{S}_u^{(B)} &= \left[|1\rangle^{(B,\sigma)}, |2\rangle^{(B,\sigma)}\right] \boldsymbol{\sigma}_u \left[\langle 1|^{(B,\sigma)}, \langle 2|^{(B,\sigma)}\right]^T, \end{aligned} \tag{16}$$

where $u = x, y$, or z, and $\boldsymbol{\sigma}_u$ is a Pauli matrix. We define the correlator

$$\hat{I} = \hat{A} \otimes \hat{B} - \hat{A} \otimes \hat{B}' + \hat{A}' \otimes \hat{B} + \hat{A}' \otimes \hat{B}', \tag{17}$$

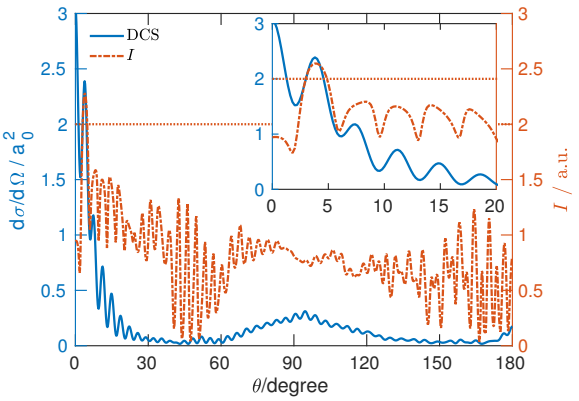

Figure 14: Differential cross section and correlator I of Eq. (17) for scattering from $\mathrm{NO}(1/2, f, m = +1/2) + \mathrm{O}_2(N_{\mathrm{O}_2} = 1, j_{\mathrm{O}_2} = 0)$ to $\mathrm{NO}(7/2, f) + \mathrm{O}_2(N_{\mathrm{O}_2} = 1, j_{\mathrm{O}_2} = 1)$.

the expectation value of which, $I = \langle \hat{I} \rangle$, satisfies the CHSH inequality $I \leq 2$ for local realistic theories. The operators $\hat{A}$, $\hat{A}'$, $\hat{B}$, and $\hat{B}'$ are the spin operators, defined above, along some directions, for example $\hat{A} = \boldsymbol{a} \cdot \hat{\boldsymbol{S}}^{(A)}$ for some unit vector $\boldsymbol{a}$ that defines the measurement direction. The "measurement angles" for all four operators can be optimized to maximize the expectation value of Eq. (17) in an attempt to find violations of the Bell inequality $I \leq 2$. The above provides an abstract definition of the optimized measurements, which in principle can be expressed in terms of angular momentum polarization and alignment moments.[21] A hypothetical experimental Bell test would require performing these optimized measurements in coincidence for both molecules.

In the special case $d_A = d_B = 2$, the above corresponds to the choice of measurement of Gisin,[22] and it can be shown that the CHSH inequality $I \leq 2$ is violated if, and only if, the second singular value is non-zero and hence the wave function is entangled. In this sense, the present choice of measurement is optimal – for a given wave function – for finding violations of Bell inequalities. Our choice of measurement generalizes in the case $d_A > 2$ and/or $d_B > 2$ as the third and higher singular states are eigenstates at eigenvalue zero. These states do not contribute to the expectation value of Eq. (17), and this choice could be improved upon, exploiting quantum correlations expressed in the third and higher singular vectors. For simplicity, we use the approach outlined above, and show that this is indeed sufficient to find violations of Bells inequality for dimensions $d_< > 2$.

Figure 14 shows the differential scattering cross section for scattering to $\mathrm{NO}(7/2, f) + \mathrm{O}_2(N_{\mathrm{O}_2} = 1, j_{\mathrm{O}_2} = 1)$, along with the quantity I, which violates the CHSH inequality $I \leq 2$ at a specific scattering angle. The singular vectors used in the definition of the measurements, Eq. (16), have been calculated for the scattering wave function at the "Fraunhofer peak", the first peak in the pattern of diffraction oscillations. The "measurements angles" have been optimized numerically for each scattering angle. The expectation value of the correlator, I, shows oscillations that are in phase with the diffraction oscillations. This can be understood from

the analytic Fraunhofer theory of diffraction oscillations,[23] which explains the amplitude and spacing of diffraction oscillations in m-resolved sub-states. The quantity I measures correlations in the scattering wave function using a measure that was optimized for scattering to the specific substate that dominates the Fraunhofer peak, and hence shows revivals at the maxima in the diffraction oscillations. The sub-state purity is largest at the Fraunhofer peak, which is why the correlator, I, is largest here, and violates the CHSH inequality.

References

[1] Onvlee, J., Vogels, S. N., von Zastrow, A., Parker, D. H. & van de Meerakker, S. Y. T. Molecular collisions coming into focus. *Phys. Chem. Chem. Phys.* **16**, 15768–15779 (2014).

[2] Vogels, S. N. *et al.* Imaging resonances in low-energy NO - He inelastic collisions. *Science* **350**, 787–790 (2015).

[3] Yan, B. *et al.* A new high intensity and short-pulse molecular beam valve. *Rev. Sci. Instrum.* **84**, 023102 (2013).

[4] Townsend, D., Minitti, M. P. & Suits, A. G. Direct current slice imaging. *Rev. Sci. Instrum.* **74**, 2530–2539 (2003).

[5] von Zastrow, A. *et al.* State-resolved diffraction oscillations imaged for inelastic collisions of NO radicals with He, Ne and Ar. *Nat. Chem.* **6**, 216–221 (2014).

[6] Even, U. Pulsed supersonic beams from high pressure source: Simulation results and experimental measurements. *Adv. Chem.* **2014**, 1–11 (2014).

[7] Western, C. M. PGOPHER: A program for simulating rotational, vibrational and electronic spectra. *J. Quant. Spectrosc. Radiat. Transfer* **186**, 221–242 (2017).

[8] Mizushima, M. *The Theory of Rotating Diatomic Molecules* (Wiley, New York, 1975).

[9] The MathWorks, Inc. MATLAB (2017).

[10] Karman, T., van der Avoird, A. & Groenenboom, G. C. Communication: Multiple-property-based diabatization for open-shell van der waals molecules. *J. Chem. Phys.* **144**, 121101 (2016).

[11] de Jongh, T. *et al.* Imaging diffraction oscillations for inelastic collisions of NO radicals with He and D_2. *J. Chem. Phys.* **147**, 013918 (2017).

[12] Boys, S. & Bernardi, F. The calculation of small molecular interactions by the differences of separate total energies. some procedures with reduced errors. *Mol. Phys.* **19**, 553–566 (1970).

[13] Alexander, M. H. Adiabatic and approximate diabatic potential energy surfaces for the B...H_2 van der waals molecule. *J. Chem. Phys.* **99**, 6014–6026 (1993).

[14] Kłos, J. A., Ma, Q., Alexander, M. H. & Dagdigian, P. J. The interaction of NO($X^2\Pi$) with H_2: Ab initio potential energy surfaces and bound states. *J. Chem. Phys.* **146**, 114301 (2017).

[15] Wormer, P. E. S., Kos, J. A., Groenenboom, G. C. & van der Avoird, A. Ab initio computed diabatic potential energy surfaces of ohhcl. *J. Chem. Phys.* **122**, 244325 (2005).

[16] Kirste, M. *et al.* Quantum-state resolved bimolecular collisions of velocity-controlled OH with NO radicals. *Science* **338**, 1060–1063 (2012).

[17] Lanza, M. & Lique, F. Hyperfine excitation of linear molecules by para- and ortho-H_2: Application to the HCl-H_2 system. *J. Chem. Phys.* **141**, 164321 (2014).

[18] Bell, J. S. On the einstein podolsky rosen paradox. *Physics* **1**, 195 (1964).

[19] Collins, D., Gisin, N., Linden, N., Massar, S. & Popescu, S. Bell inequalities for arbitrarily high-dimensional systems. *Phys. Rev. Lett.* **88**, 040404 (2002).

[20] Zhao, M.-J., Ma, T., Fei, S.-M. & Wang, Z.-X. Inequalities detecting quantum entanglement for $2 \bigotimes d$ systems. *Phys. Rev. A* **83**, 052120 (2011).

[21] Suits, A. G. *et al.* Direct extraction of alignment moments from inelastic scattering images. *J. Phys. Chem. A* **119**, 5925–5931 (2015).

[22] Gisin, N. Bell's inequality holds for all non-product states. *Phys. Lett. A* **154**, 201 (1991).

[23] Onvlee, J. *et al.* Imaging quantum stereodynamics through fraunhofer scattering of NO radicals with rare gas atoms. *Nat. Chem.* **9**, 226 (2016).